# Printable Programmable Viscoelastic Materials for Robots

Robert MacCurdy*, Jeffrey Lipton*, Shuguang Li and Daniela Rus

*Abstract*— Impact protection and vibration isolation are an important component of the mobile robot designer's toolkit; however, current damping materials are available only in bulk or molded form, requiring manual fabrication steps and restricting material property control. In this paper we demonstrate a new method for 3D printing viscoelastic materials with specified material properties. This method allows arbitrary net-shape material geometries to be rapidly fabricated and enables continuously varying material properties throughout the finished part. This new ability allows robot designers to tailor the properties of viscoelastic damping materials in order to reduce impact forces and isolate vibrations. We present a case study for using this material to create jumping robots with programmed levels of bouncing.

## I. INTRODUCTION

Robots have to cope with various situations that require damping in locomotion and manipulation. For locomotion, bouncing can help propel the robot to the next step [1] although in other applications landing with minimal rebounds ("sticking the landing") is important. When manipulating vibrating tools it is desirable to absorb the vibrations of the tools. In this paper we present and analyze a new fabrication method for materials whose viscoelastic properties can be specified in software and realized automatically; in other words the mechanical properties can be programmed. We then apply this approach to building jumping robots whose bodies can absorb the forces generated upon contact with the ground. Our method is a 3D printed approach that combines the printing of solids with liquids to achieve materials with graded viscoelastic properties. These materials have a storage modulus $E' \in \{0.1, ..., 1\}$ MPa and a tangent delta $tan(\delta) \in \{0.2, ..., 0.9\}$, at 1Hz. We use a data-driven approach to develop a model for the placement of solid and liquid droplets deposited by a 3D inkjet printer that will achieve a desired mechanical property within this range, and we measure the mechanical properties of these printed materials. Finally, we use these materials to create a new jumping cube robot that can "stick the landing".

In this paper we contribute:

- A new fabrication method for printing viscoelastic materials
- Data-driven models that describe the mechanical properties of these materials

*These authors contributed equally to this work

Authors are from the Computer Science and Artificial Intelligence Laboratory, Massachusetts Institute of Technology, The Stata Center, Building 32, 32 Vassar Street, Cambridge, Massachusetts 02139, USA (`maccurdy, jlipton, lisg, rus`)`@mit.edu`

- Algorithms for generating the printable material design files
- Measurements that characterize these materials in dynamic low- and high-strain regimes.
- A comparative study of the application of these materials to a jumping robot

### A. Prior Work

Soft and hard jumping robots have been made for a wide variety of purposes but none have used custom viscoelastic damping to improve their performance and durability. The "Sand Flea" robot launches itself over obstacles with a pressurized air cannon, and uses its rigid plastic wheels to absorb the impact [2]. Others such as the Mowgli use an articulated spring system on legs to absorb the impact forces [3]. The Jollbot encloses the entire lightweight robot into a much larger cage, limiting the space it can fit into and requiring it to operate in a smooth environment to ensure nothing penetrates the cage [4]. Soft robots can sustain large falls and hard impacts due to their light weight and lack of rigid structure [5]. Their elastomeric bodies can easily deform without damage but can flail on impact causing them slide off of their targets. [6].

Power sources such as motors and pumps can shake a system adding unwanted noise and dynamics [7],[8],[9],[10],[11]. This can lead robots to be difficult to control. Traditionally discrete spring mass damper systems have been used to adjust vibration responses in larger structures [12]. Others have used active acoustic cancellation to eliminate vibrations in structures [13]. However, simple passive damping materials are the most commonly used and robust approach to reduce vibrations [14], [15], yet these materials are only commercially available with specific material properties and dimensions.

## II. BACKGROUND

Dampers are energy-absorbing elements that convert mechanical work into heat, dissipating that thermal energy in the ambient environment. Energy dissipating dampers can be implemented in various ways through the use of liquid (hydraulic), gas (pneumatic), and viscoelastic (rubber, plastic, foam) materials. Dampers based on gasses or liquids force the working fluid through an orifice, causing flows that generate heat. Because they must constrain the working fluid, devices based on this principle usually contain multiple parts including sliding seals and cylinders, which contribute to component cost and size [16]. In contrast, viscoelastic materials are inherently dissipative: they have a stress-strain relationship that exhibits a phase lag, creating a hysteretic

loop [17]. This relationship can be seen in Equation 1, where $\sigma$ is stress, $\varepsilon$ is strain, and the Young's modulus, $E^*$, is represented as a complex number. $E'$ represents the in-phase response of the material and is known as the storage modulus. It is the component of $E^*$ that stores and releases energy when compressed. $E''$ is the loss modulus which represents the out of phase dissipative response of the material to deformation.

$$\sigma = \varepsilon E^*, E^* = E' + iE'' \qquad (1)$$

Viscoelastic materials are widely used as dampers because they are simple, compact, inexpensive, and widely available; most natural rubbers are viscoelastic. As bulk materials, they can be shaped into the desired net geometry by conventional methods (casting, cutting/stamping, extruding, heat-forming, molding etc). However, this simplicity comes at a cost. The tooling required to create the desired geometry can be time-consuming to setup, and the materials have isotropic material properties; if regions with varying stiffness or damping are desired, they must be implemented with physically different pieces of material, placed adjacent to each other.

Additive manufacturing (3D printing) provides a means to overcome these limitations. By providing a mechanism for simultaneously depositing different materials (with different mechanical properties) within a design, multi-material additive manufacturing allows computer code to specify the mechanical properties of every region of a part using a new composite "Programmable Material". This new material can have mechanical properties that vary continuously as a function of position by controlling the proportions of each constitutive element.

## III. USING THIS METHOD

We recently showed that a commercially available inkjet 3D printer could be modified to simultaneously print with different solid and liquid materials. We used the liquid material, within a rigid shell, as a force-transmitting element via hydraulic pressure [18]. In this paper we use a similar approach to configure the printer (Objet Connex 260, Stratasys Corp.), but employ continuous distributions of a flexible material (TangoBlack+, Stratasys Corp.) and a liquid material (Model Cleaning Material, Stratasys Corp.) by depositing adjacent droplets of each material type. Multi-material objects fabricated in this manner are specified by an occupancy matrix in $\mathbb{R}^3$. The entries of this matrix correspond to the voxels of the part that will be built. Materials with mechanical properties that differ from the base materials (in this case, TangoBlack+ and liquid) can be specified by assigning different fractions of randomly chosen voxels to one material type or the other, assuming that the chosen voxels lie within the bounding surface of the part (STL file) that will be fabricated, according to Algorithm 2. This approach allows customized printed viscoelastic materials (PVMs) to be designed and fabricated using modifications of an existing toolset.

This method is used according to Algorithm 1. We provide an overview here; specific examples of impact-absorbing

applications and vibration isolation are shown in sections V-A and V-B. First, the designer must determine whether the viscoelastic material is likely to be used in small ($\varepsilon < 0.01$) or large deformations ($\varepsilon > 0.01$). Vibration damping applications will typically fall into the former category, while impact absorbing cases fit the latter. Next, the desired material property is chosen, and the liquid percentage that determines it is obtained in the following way.

In the small deformation regime ($\varepsilon < 0.01$), $E^*$ is a complex function of frequency and liquid percentage, as shown in Equation 2. $E^*$ can be expanded, using the parameters and models from Table II. Note that when expanding Equation 5, the constant values $a$, $b$, $c$, and $d$ are model-specific and must be read from the corresponding row of the table. Similarly, the models for $n_1$ and $n_2$ are specific to the liquid concentration used. Equation 5 cannot be algebraically solved for $P_l$, but can be numerically evaluated across the range of its inputs $\omega \in [0,...,2\pi*100]$, $P_L \in [0,...,50]$, and then satisfying liquid percentages can be read from a lookup table.

We chose to characterize the coefficient of restitution for impact applications (large deformation regime, $\varepsilon > 0.01$), since $e^*$ is defined as the ratio of energy in an object before and after a collision. Equation 6 shows the model for PVMs in this application, which may be evaluated to return the required $P_l$ for a desired $e^*$.

The liquid percentage is used, along with a user-generated object outline STL file, as an input to Algorithm 2, yielding the occupancy matrix $M(v)$. $M(v)$ is an element-by-element list of all voxels in the printer's build envelope, and identifies which material type will be deposited in each possible voxel. The voxels define the minimum resolution of the printer. Finally, $M(v)$ is converted into the surface files (STL format, one per material) used to print the part.

The present method uses $P_l$ as the only determining property of the printed material. Algorithm 2 works by randomly assigning a certain percentage of the voxels in the part to the liquid, and the rest to the solid. This approach produces a material with isotropic mechanical properties. Though we do not include them here, other variations of this algorithm yield voxel distributions that lead to interesting anisotropic material properties.

---

**Algorithm 1** Procedure to use this method

1: **if** Small strain **then**
2:     Choose desired $E'$, $E''$ or $tan(\delta)$
3:     Compute $P_l$ numerically from Equation 5 and Table II
4: **else if** Large strain **then**
5:     Choose desired $e^*$ or $F_t$
6:     Compute $P_l$ numerically from Equation 6
7: **end if**
8: Generate a desired object shape using CAD tools and export an STL file
9: $M(v) \leftarrow Algorithm\ 2(STL, P_l)$
10: Convert $M(v)$ into constitutive STL files
11: Print STL files

---

**Algorithm 2** Calculate $M(v) \in \mathbb{R}^3$, given $STL$ and $P_l$

1: **for all** voxels $v$ in $M$ **do**
2:   **if** $v$ is inside $STL$ **then**
3:     $r \leftarrow random \in [0,1]$
4:     **if** $r > Pct$ **then**
5:       $M(v) \leftarrow Material\ A$
6:     **else**
7:       $M(v) \leftarrow Material\ B$
8:     **end if**
9:   **else**
10:     $M(v) \leftarrow Empty$
11:   **end if**
12: **end for**

TABLE I

VARIABLE NAMES AND DEFINITIONS

| Variable Names | |
|---|---|
| $E^*$ | Complex Young's Modulus |
| $E'$ | Storage Modulus |
| $E''$ | Loss Modulus |
| $\sigma$ | Stress |
| $\varepsilon$ | Strain |
| $E_0$ | Impacter energy before collision |
| $\Delta E$ | Change in impacter energy |
| $e^*$ | Coefficient of restitution $e^* \equiv \Delta E / E$ |
| $F_t$ | Peak transmitted force |
| $tan(\delta)$ | $tan(\delta) \equiv E''/E'$ |
| $\omega$ | Frequency (rad/sec) |
| $i$ | Imaginary number $i \equiv \sqrt{-1}$ |
| $P_l$ | Percent liquid by volume in a material $P_l \in [0,...,100]$ |
| $a, b, c, d$ | Model-fit constants |
| $A_0$ | Undeformed cross-sectional area of sample |
| $L_0$ | Undeformed length of sample |
| $M(v)$ | Occupancy matrix defining voxel material assignments in the printed part |

## IV. MODELING

The 3D printer deposits droplets of UV-cured resin creating voxels that are approximately 30 x 30 x 40 $\mu$m (X,Y,Z). When non-curing liquids and UV-curing materials are in close proximity, as they would be during the fabrication of a PVM with high liquid concentration, pre-curing mixing between these materials is likely to occur. It is also likely that some fraction of the liquid is absorbed into the solid soon after printing. Therefore, although the 3-dimensional pattern of voxels is prescribed by $M(v)$, the microscopic structure of the 3D printed materials realized by this method is currently unknown. Additionally, modeling viscoelastic materials with a bottom-up approach, based on finite elements or lumped parameters is an active area of research and is application-specific [19], [20]. Though developing a material model from first-principles would be

an interesting area of research, in this paper we chose to characterize the achievable material properties experimentally, and used those measurements to build phenomenological models of the material for impact- and vibration-absorbing applications (see Table II and Equations 2 - 6).

### A. DMA Measurements

In order to characterize the material's response to vibrations, we tested printed samples on a TA Q800 Dynamic Mechanical Analyzer (DMA). Five samples of each concentration were printed on a Connex 260 3D printer for testing. We 3D printed samples at 0 through 50% liquid concentrations in increments of 5%. Each sample was 10 mm in diameter and 10 mm tall, in accordance with DIN 53 513. The samples were tested in accordance with ASTM standard D5992-96. Test frequencies were varied from 1 Hz to 100 Hz on an evenly spaced log scale of frequencies with 10 frequencies per decade. Each sample was compressed 75$\mu$m at 22°C.

As seen in Figure 1(a) and 1(b) the storage modulus $E'$ and loss modulus $E''$ lie along lines in a loglog plot for all of the frequencies and liquid concentrations tested. This clearly shows that there is a power law relationship of the form of Equation 2. Each line varies in slope, indicating that there is a different power law exponent for each of the concentrations of liquid. The higher slopes of the fits in Figure 1(b) shows that there is a faster increase in $E''$ with frequency than $E'$. If we can model $E'$ and $E''$ at 1 Hz, and the power law exponents $n_1$ and $n_2$, as a function of the liquid concentration, we are able to predict the value of $E^*$ at any frequency greater than 1 Hz. Figure 1(c) and 1(d) show that both moduli can be fit to a model in terms of the liquid concentration. The model is a function of $P_l$ of the form $ae^{bP_l} + ce^{dP_l}$. The coefficients $a, b, c, d$ can be found in Table II.

$$E^*(\omega, P_l) = E'(\omega, P_l) + i * E''(\omega, P_l) \qquad (2)$$
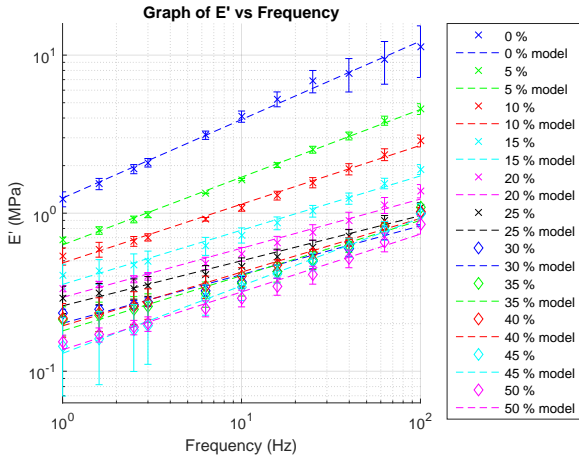$$E'(\omega, P_l) = E'|_{1Hz} * \omega^{n_1} \qquad (3)$$
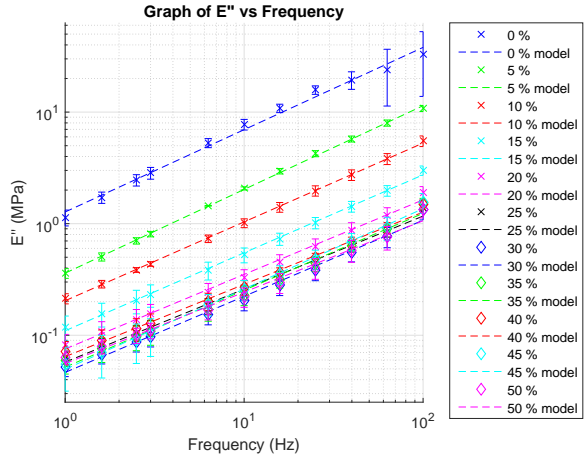$$E''(\omega, P_l) = E''|_{1Hz}\omega^{n_2} \qquad (4)$$
$$E^*(\omega, P_l) = E'|_{1Hz} * (\omega^{n_1} + i * tan(\delta)|_{1Hz}\omega^{n_2}) \qquad (5)$$
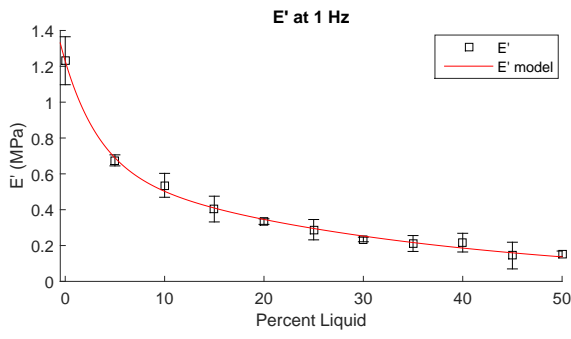
(see Table II for $n_1, n_2$)

We can see in Figures 1e and 1f that the relationship of $n_1$ and $n_2$ with $P_l$ are modeled differently for concentrations below 25% and above 25%. This suggests a physical change in the material at 25%. Modeling the power terms as linear ($E''$) or quadratic ($E'$) with $P_l$ when $P_l \leq 25\%$, produces an acceptable fit, while the linear model for behavior above 25% does not hold. The coefficients of the models can be seen in Table II. We observed under optical magnification that at liquid concentrations below 25%, PVMs look like a single soft material, while at concentrations above 25% liquid films form on their surface and the PVMs slowly leak liquid over time. We were not able to directly observe, but we hypothesize that at liquid concentrations higher than 25% PVMs form an open-cell foam, providing an exit path
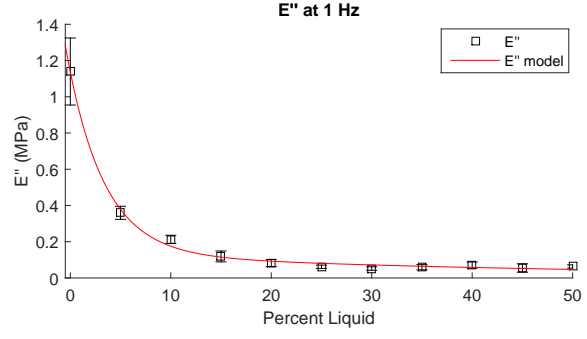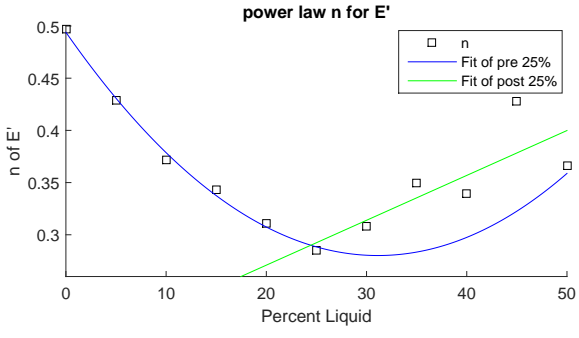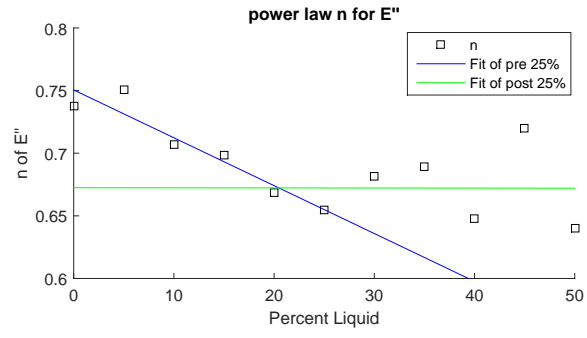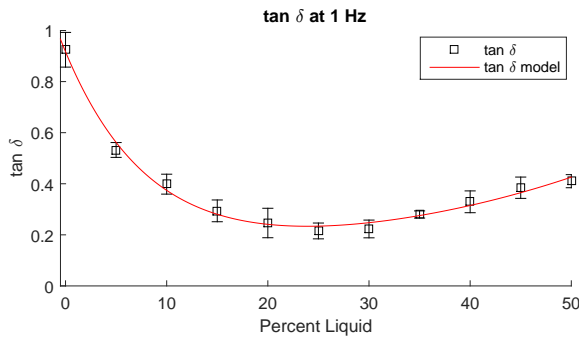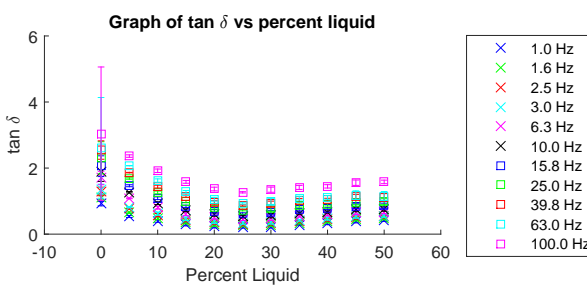
Fig. 1. The complex modulus of the material varies as a function of liquid percentage. The storage modulus $E'$ (a) and loss modulus $E''$ (b) can be modeled as a power law function of frequency for all of the material concentrations tested. The power exponent n for the storage modulus (e) loss modulus (f) can be fit as two different models which switch at 25% concentration. The value of $E'$ at 1 Hz (c) and $E''$ at 1Hz can be modeled as a function of percentage liquid. The tan$\delta$ at 1 Hz (g) can be modeled and applied over the range of frequencies (h)

TABLE II

THE PHYSICAL PROPERTIES OF THE COMPLEX MODULUS $E^*$ CAN BE
MODELED AS A FUNCTION OF $P_l$

| Physical Property | Physical Property Model | a | b | c | d | Range of $P_l$ |
|---|---|---|---|---|---|---|
| $E'\|_{1Hz}$ | $ae^{bP_l}+ce^{dP_l}$ | 0.595 | -0.282 | 0.635 | -0.031 | 0%-50% |
| $E''\|_{1Hz}$ | $ae^{bP_l}+ce^{dP_l}$ | 1.00 | -0.272 | 0.135 | -0.021 | 0%-50% |
| $tan(\delta)\|_{1Hz}$ | $ae^{bP_l}+ce^{dP_l}$ | 0.832 | -0.118 | 0.085 | 0.032 | 0%-50% |
| $n_1$ of $E'$ | $aP_l^2+bP_l+c$ | $2.21e^{-4}$ | $-1.37e^{-2}$ | 0.494 | - | 0%-25% |
| $n_2$ of $E$" | $aP_l+b$ | $-3.82e^{-3}$ | $7.51e^{-1}$ | - | - | 0%-25% |
| $n_1$ of $E'$ | $aP_l+b$ | $4.30e^{-3}$ | $1.85e^{-1}$ | - | - | 25%-50% |
| $n_2$ of $E$" | $aP_l+b$ | 0 | $6.73e^{-1}$ | - | - | 25%-50% |

for the deposited fluid. This could provide one explanation for the different models required above and below the 25% concentration.

From these results we can conclude that printable viscoelastic materials (PVM) can be modeled as a soft glassy material (SGM) because the storage and loss moduli of SGM materials have a power law relation with frequency [21]. The high value of $n_1$ and $n_2$ (see Table II) also indicate that the materials should not have a significant aging effect [21].

In order to simplify calculations it is convenient to replace $E''\|_{1Hz}$ with $E'\|_{1Hz} * tan(\delta)\|_{1Hz}$. This allows us to combine Equations 2, 3, and 4 to get Equation 5. Figure 1(g) shows that $tan(\delta)\|_{1Hz}$ can be modeled by a double exponential function as well.

### B. Impact Measurements

In contrast to the low-strain, controlled-rate cyclic testing performed on the DMA, impact loads are often rapid, high magnitude, one-time events. In order to characterize the impact protection that PVMs could provide, we performed impact tests using a custom built testing apparatus. The test consisted of 44.4g or 223g masses suspended from nylon lines that were dropped from predetermined heights at samples which were mounted on a quartz crystal force sensor. The sensor, sampled at 48 kHz by at 14 bit USB DAQ card, was attached to a granite slab to ensure there was no compliance in the sensor mount. Test PVM samples were 63.5 mm in diameter ($A_0 = 3.17e^{-3}$ m$^2$), 12.7 mm in height ($L_0 = 1.27e^{-2}$ m). The masses were dropped from heights of 100 mm through 500 mm in increments of 100 mm. High speed videos (1820 fps) of the impact were collected via an Edgertronic high speed camera and processed in MATLAB to determine incoming and outgoing velocities of the masses. The coefficient of restitution $e^* = |V_{out}/V_{in}|$ was calculated from the processed video data and plotted against $P_l$ for the nine different impact energy cases in Figure 2 (a). A quadratic model, shown in Equation 6, fit this data with a standard error of $RMSE = 0.0136$ and yields a mapping between the coefficient of restitution in impacts, $e^*$, and $P_l$.

As seen in Figure 2, the coefficient of restitution finds a minimum in the range of 4% to 10% liquid concentration,

indicating that this range of liquid concentration yields materials with the highest energy absorption. The peak impact force on the sample is directly correlated with the stiffness of the sample. Since we can model the sample as a spring with $k \propto E^*$ the stopping distance of the impacting mass should be inversely proportional to $E^*$ and the force is inversely proportional to the stopping distance. Therefore the weaker samples which we can produce at high liquid concentrations provide lower peak forces (and presumably greater impact penetration distances). Figure 2 shows a decrease in peak force with liquid concentration as expected.

$$e^* = p1P_l^3 + p2P_l^2 + p3P_l^1 + p4 \quad (6)$$
$$p1 = -1.23e^{-5}, \ p2 = 8.05e^{-4}, \ p3 = -8.55e^{-3}, \ p4 = 1.5e^{-1}$$

The reduction in peak force can be a significant protection for mobile robots. In our experiments, we see a 700N reduction in peak force by varying from 0% to 25% liquid concentration. This can be the difference in a circuit surviving a shock, a sensor lens cracking upon impact with the ground, or a strut breaking off of a quadrotor. While traditional elastomers can be placed on robots for protection, their high level of recoil can lead to the object simply bouncing off the ground in an uncontrolled manner, causing further damage. A gradual stop without high recoil is preferred to protect any robot from both planned and unplanned ground contact. The programmable relationship between $e^*$ and peak force, allows designers of mobile robots to make a tradeoff between recoil and peak force.

## V. APPLICATIONS

### A. Impact Protection for a Jumping Robot

We used our recent jumping robot [1] to demonstrate the utility of PVMs in this application by printing impact absorbing skins. 3D printing these parts allowed more rapid development of the skin than was possible during the original fabrication, which involved printing molds and casting a commercially available elastomer (Soma Foama, Smooth-On Corp.). Our robot has a cubic shape, and each of its six faces has an opening to allow the jumping mechanism to make contact with the ground. By winding up and releasing a strip spring, the robot can jump in two directions, regardless of orientation. The robot has a main rigid body, 3D printed using ABS materials, that houses the actuation, control, and power. The rigid body is then encased in a soft skin for landing. We used 4 layers of looped metal strip as the spring in each half of our robot. The strips are made of stainless steel 316, and they are 12.7 mm wide, 0.254 mm thick, and 60 mm long. We used two micro DC gear motors (1.1 N-m) to drive the metal strips. The microcontroller (Arduino Pro Micro, 3.3V/8MHz), rechargeable battery (3.7V, 400 mAh), regulator (9V), motor driver (DRV8833), wireless communication module (XBee 1mW, 2.4G Hz), and 9-axis IMU sensors (L3GD20H and LSM303D) are mounted within the space between the bottom plates of two halves.
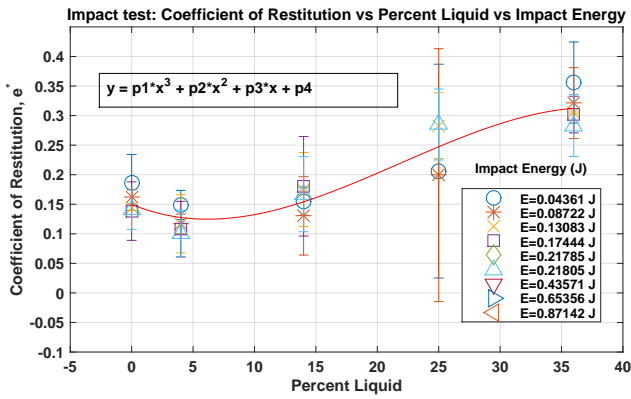
(a)
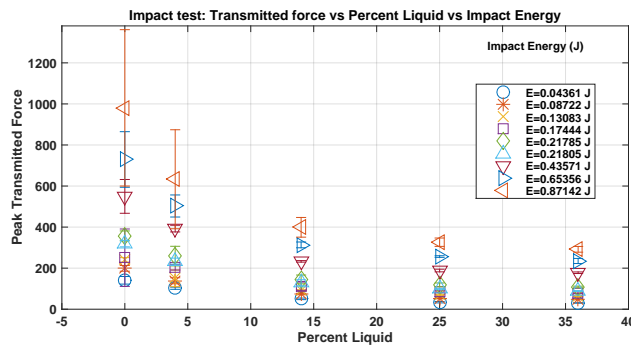


(b)

Fig. 2. Impact test results. Nine different mass/drop height combinations were used with 5 sample types. The coefficient of restitution (a) and the force transmitted through the sample (b) and are shown, along with a curve fit for $e^*$. Notice that the amount of energy absorbed by the sample reaches a maximum when the sample contains $\approx 6$ percent liquid. Sample types: {0=100% TangoBlack+; 4=96% TangoBlack+, 4% liquid; 14=86% TangoBlack+, 14% liquid; 25=75% TangoBlack+, 25% liquid; 36=64% TangoBlack+, 36% liquid}

We fit this jumping robot with different PVM skins ($P_l \in [0\%, 18\%, 25\%, 36\%]$) and compared them to the original elastomeric foam design. We used the accelerometer inside the robot to measure the peak acceleration (as a proxy for likely damage) and the number of bounces after each jump. By minimizing acceleration, a designer can predict that the robot will have a longer cycle life before failure. Additionally, a lower peak acceleration on landing reduces the damage to the surface the robot lands on. The number of bounces after landing serves as a metric for the maintenance of orientation and position during the landing process.

All of the printed skins outperformed the original elastomeric foam on peak acceleration and number of bounces. Figure 4 shows that the peak acceleration can be reduced by half with an 18% liquid concentration. From the data we can conclude that the PVM reduces the number of bounces and decreases the acceleration compared to the elastomer, but we cannot determine a clear trend within the PVMs with respect to peak acceleration. In fact, it appears that peak acceleration actually increases slightly with concentrations above 18%. This could be because the higher liquid concentrations cause the robot to bottom out upon landing. The 36% has a $E'|_{1Hz}$

which is nearly half the 18% value. The lower resulting $K$ value should double the stopping distance and halve the peak force, unless the impact-absorber bottoms out, which would transfer the remaining impact to the rigid inner skeleton. These results suggest that the concentrations need to be tailored not only for minimum spring constants, but also for the allowable compression distances.
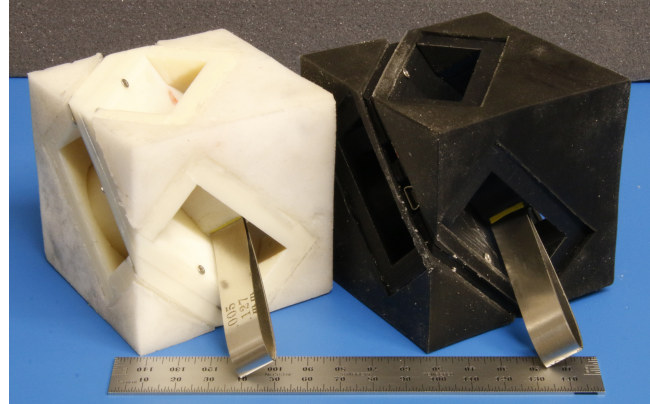


Fig. 3. Jumping robots from [1]. A motor rotates and compresses a spring-steel leg, propelling the robot. A vibration-absorbing skin assists landing.
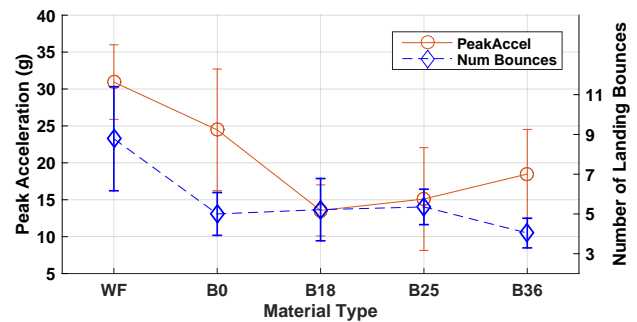


Fig. 4. Impact absorbing skin test on a jumping robot. By applying a 3D-printed skin to a jumping robot the peak acceleration and number of landing bounces can be reduced, relative to a commercially-available bulk material. WF=SomaFoama 25; B0=100% TangoBlack+; B18=82% TangoBlack+, 18% liquid; B25=75% TangoBlack+, 25% liquid; B36=64% TangoBlack+, 36% liquid

We compared the performance of two cubes fitted with $P_l =18\%$ PVM and elastomer skins by commanding the cubes to repeatedly jump from the same location, in the same direction. The reduced bouncing observed with the PVM skin leads to a more consistent landing pattern. Figure 6 shows that the PVM cube traveled a shorter distance than the elastomer cube, though in a more consistent manner. The elastomer-skinned cube bounces and rolls farther with each jump than the same cube with a PVM skin, but it has a larger variance in its final position. The results in Figure 6 demonstrate that the PVM skins help to reduce the landing point uncertainty.

### B. Vibration Isolation

Since we can model the complex modulus $E^*$ of the material as a function of $P_l$ we can design transfer functions
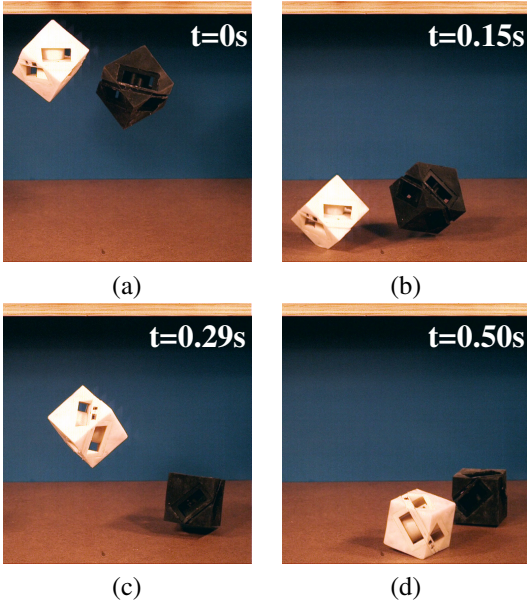
Fig. 5. An elastomer cube (red) and a PVM cube were dropped from the same height (a) and landed on their corners (b). In contrast to the PVM cube, the elastomer cube rebounded several body-heights (c) before both cubes settled (d).
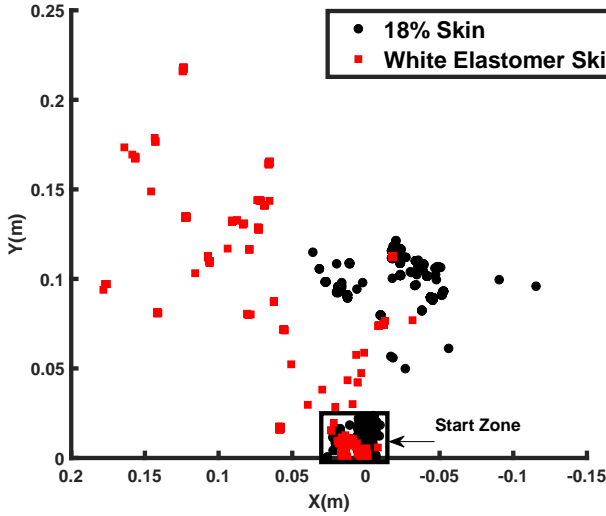


Fig. 6. An elastomer cube (red squares) and a PVM cube with 18% liquid(black) jumped from the same starting position. Points near (0,0), inside the starting square, are the starting locations. The black cube lands in a more predictable area than the elastomer cube

for vibrating systems of different sizes and masses. Here we provide two common vibration-isolation examples: base excitation and disturbance rejection (see Figure 7). The standard formulation for the spring constant of a bar of homogeneous material is given in equation 7. Combining equations 7 and 5 yields the complex spring constant of the form in equation 8. We can then model a mass $m$ with a complex spring and base excitation as a difference between the base position $x(t)$ and the mass position $y(t)$ seen in equation 9. We assume a solution of the form $y(t) = Y \exp(i\omega t), x(t) = X \exp(i\omega t)$ and get the transfer function in Equation 10.
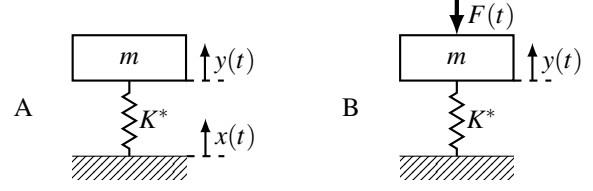


Fig. 7. Two vibration-isolation examples employing PVM. A: Isolating from a moving mount/base. B: Minimizing disturbance distance due to an external force.

$$K = \frac{A_0}{L_0}E \qquad (7)$$

$$K^* = \frac{A_0}{L_0}E'|_{1Hz}(\omega^{n_1} + i*tan(\delta)|_{1Hz}*\omega^{n_2}) \qquad (8)$$

$$m\ddot{y} + K^*(P_l)*(y-x) = 0 \qquad (9)$$

$$T_{base}(\omega, m, K^*) = \frac{Y}{X} = \frac{K^*(P_l)}{m\omega^2 + K^*(P_l)} \qquad (10)$$

$$m\ddot{y} + K^*(P_l)*y = F(t) \qquad (11)$$

$$F(t) = F_0*cos(\omega_d t) \qquad (12)$$

$$T_{driven}(\omega_d, m, K^*) = \frac{Y}{F} = \frac{1}{m\omega_d^2 + K^*(P_l)} \qquad (13)$$

This leads to a system with 3 free parameters, $A_0$, $L_0$ and $P_l$ to control a magnitude of oscillation for a system of mass m. In Figure 8 we see a characteristic transfer function magnitude for a system with a 44.4g mass, 63.5mm diameter and 12.7mm thickness. We can see that regardless of the liquid concentration, the material is highly damped, leading to little response at any resonant frequency. However, in this example materials with higher $P_l$ yield better performance at higher frequencies.

In the disturbance-rejection example, if the driving force is of the form in equation 12, and the position of the mass is defined at $y(t)$, then the dynamics are described by Equation 11. The transfer function between force and displacement ($T_{driven}$) is of the form 13. Only $K^*$ is a free variable that describes the magnitude of the transfer function. $K^*$ itself a function of the area and length of the spring, and the complex modulus, as described in Equation 8. Specifying the size of the spring leaves only the complex modulus $E^*$ as a free parameter in the system and it is a function of $P_l$ alone. To prevent the system from bottoming out one must minimize the transfer function such that $\frac{m*g+F_0}{K} > 0.5*L_0$, where g is the strength of gravity.

## VI. CONCLUSIONS

We have presented an accessible and scalable technique for designing and fabricating user-defined viscoelastic damping materials using commercially-available 3D printers and materials. The process allows customized viscoelastic dampers to be automatically fabricated in arbitrary shapes. Rather than printing complex multi-part molds, selecting materials, and then fabricating a custom part in the lab, robot designers can
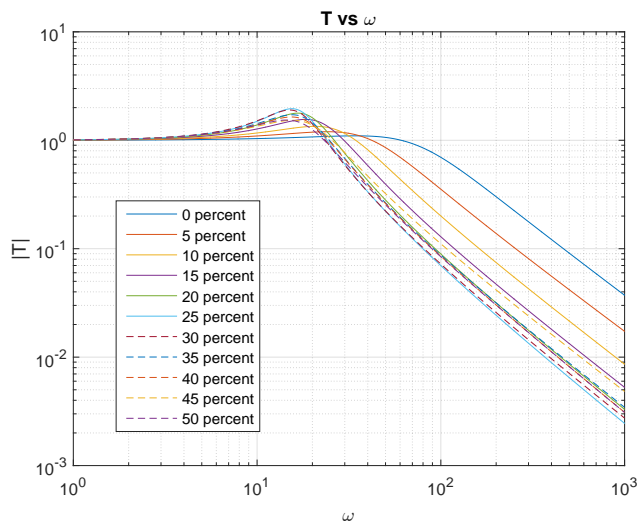
Fig. 8. The transfer function magnitude can be controlled by varying the percent liquid concentration of the material

now optimize the material properties and directly 3D print their custom soft damper parts.

Our model of the material allows designers to determine the correct liquid concentration for the desired $E'$ and $E''$ properties and frequency response of the material. By taking into account the working space, the spring constant can be optimized to reduce the impact force and recoil. For vibrating systems, the transfer function of the mass-spring system can be minimized against the frequency range, maximum displacements and mass.

There are many potential applications in the robotics community. For example, this technique could make it possible to design grippers with printable PVM layers that minimize the transmitted vibrations from the end-effector to the arm, reducing actuator wear and control effort to maintain position. Customized impact protecting skins/pads based on PVMs could allow robots to be more resilient to impacts, to be more accurate when landing, and to reduce controller complexity and effort. The vibration damping properties of PVMs can be used in traditional hard robotics to protect sensitive parts such as cameras and electronics from the vibrations of motors, generators and movement. In the future this material and process may find applications in a wide range of fields, including custom sporting gear, personal protective equipment, and vibration isolation in cameras or industrial equipment.

## ACKNOWLEDGMENT

## REFERENCES

[1] S. Li, R. Katzschmann, and D. Rus, "A soft cube capable of controllable continuous jumping," in *Intelligent Robots and Systems (IROS), 2015 IEEE/RSJ International Conference on.* IEEE, 2015, pp. 1712–1717.

[2] *SandFlea spec sheet*, Boston Dynamics. [Online]. Available: http://www.bostondynamics.com/img/SandFlea%20Datasheet%20v1_0.pdf

[3] R. Niiyama, A. Nagakubo, and Y. Kuniyoshi, "Mowgli: A bipedal jumping and landing robot with an artificial musculoskeletal system," in *Proc. IEEE Int. Conf. on Robotics and Automation (ICRA 2007)*, Roma, Italy, April 2007, pp. 2546–2551 (ThC5.2).

[4] R. Armour, K. Paskins, A. Bowyer, J. Vincent, and W. Megill, "Jumping robots: a biomimetic solution to locomotion across rough terrain," *Bioinspiration & biomimetics*, vol. 2, no. 3, p. S65, 2007.

[5] R. V. Martinez, A. C. Glavan, C. Keplinger, A. I. Oyetibo, and G. M. Whitesides, "Soft actuators and robots that are resistant to mechanical damage," *Advanced Functional Materials*, vol. 24, no. 20, pp. 3003–3010, 2014.

[6] M. T. Tolley, R. F. Shepherd, M. Karpelson, N. W. Bartlett, K. C. Galloway, M. Wehner, R. Nunes, G. M. Whitesides, and R. J. Wood, "An untethered jumping soft robot," in *Intelligent Robots and Systems (IROS 2014), 2014 IEEE/RSJ International Conference on.* IEEE, 2014, pp. 561–566.

[7] B. M. Yamauchi, "Packbot: a versatile platform for military robotics," in *Defense and Security.* International Society for Optics and Photonics, 2004, pp. 228–237.

[8] J. Paulos, A. Argondizza, and E. Garcia, "Reduced weight hydraulic actuation for small mobile applications," in *50th AIAA Aerospace Sciences Meeting including the New Horizons Forum and Aerospace Exposition*, 2012, p. 137.

[9] A. D. Marchese, C. D. Onal, and D. Rus, "Autonomous soft robotic fish capable of escape maneuvers using fluidic elastomer actuators," *Soft Robotics*, vol. 1, no. 1, pp. 75–87, 2014.

[10] C. Stergiopulos, D. Vogt, M. T. Tolley, M. Wehner, J. Barber, G. M. Whitesides, and R. J. Wood, "A soft combustion-driven pump for soft robots," in *ASME 2014 Conference on Smart Materials, Adaptive Structures and Intelligent Systems.* American Society of Mechanical Engineers, 2014, pp. V002T04A011–V002T04A011.

[11] M. Raibert, K. Blankespoor, G. Nelson, R. Playter *et al.*, "Bigdog, the rough-terrain quadruped robot," in *Proceedings of the 17th World Congress, International Federation of Automatic Control*, 2008, pp. 10 823–10 825.

[12] B. Samali and K. Kwok, "Use of viscoelastic dampers in reducing wind-and earthquake-induced motion of building structures," *Engineering Structures*, vol. 17, no. 9, pp. 639–654, 1995.

[13] D. Karnopp, "Active damping in road vehicle suspension systems," *Vehicle System Dynamics*, vol. 12, no. 6, pp. 291–311, 1983.

[14] K. B. Shimoga and A. A. Goldenberg, "Soft robotic fingertips part i: A comparison of construction materials," *The International Journal of Robotics Research*, vol. 15, no. 4, pp. 320–334, 1996.

[15] E. I. Rivin, E. I. Rivin, and E. I. Rivin, *Passive vibration isolation.* Asme press New York, 2003.

[16] D. Lee and D. P. Taylor, "Viscous damper development and future trends," *The Structural Design of Tall Buildings*, vol. 10, no. 5, pp. 311–320, 2001.

[17] J. C. Snowdon, "Vibration isolation: use and characterization," *Rubber Chemistry and Technology*, vol. 53, no. 5, pp. 1041–1087, 1980.

[18] R. MacCurdy, R. Katzschmann, Y. Kim, and D. Rus, "Printable hydraulics: A method for fabricating robots by 3d co-printing solids and liquids," in *Robotics and Automation (ICRA), 2016 IEEE International Conference on.* IEEE, 2016.

[19] I. Argatov, "Mathematical modeling of linear viscoelastic impact: Application to drop impact testing of articular cartilage," *Tribology International*, vol. 63, pp. 213–225, 2013.

[20] F. Varga, M. Drzik, M. Handl, J. Chlpik, P. Kos, E. Filová, M. Rampichova, A. Necas, T. Trc, and E. Amler, "Biomechanical characterization of cartilages by a novel approach of blunt impact testing," *Physiological research*, vol. 56, p. S61, 2007.

[21] D. T. Chen, Q. Wen, P. A. Janmey, J. C. Crocker, and A. G. Yodh, "Rheology of soft materials," *Condensed Matter Physics*, vol. 1, 2010.